Quantum Hall edge states in topological insulator nanoribbons

A. Pertsova, C. M. Canali, and A. H. MacDonald

Phys. Rev. B **94**, 121409 — Published 26 September 2016

DOI: 10.1103/PhysRevB.94.121409

Quantum Hall Edge States in Topological Insulator Nanoribbons

A. Pertsova* and C. M. Canali
Department of Physics and Electrical Engineering, Linnæus University, 391 82 Kalmar, Sweden

A. H. MacDonald
Department of Physics, University of Texas at Austin, TX 78712, USA

We present a microscopic theory of the chiral one-dimensional electron gas system localized on the sidewalls of magnetically-doped Bi_2Se_3-family topological insulator nanoribbons in the quantum anomalous Hall effect (QAHE) regime. Our theory is based on a simple continuum model of sidewall states whose parameters are extracted from detailed ribbon and film geometry tight-binding model calculations. In contrast to the familiar case of the quantum Hall effect in semiconductor quantum wells, the number of microscopic chiral channels depends simply and systematically on the ribbon thickness and on the position of the Fermi level within the surface state gap. We use our theory to interpret recent transport experiments that exhibit non-zero longitudinal resistance in samples with accurately quantized Hall conductances.

PACS numbers: 73.20.r, 73.43.-f
Keywords: topological insulator thin films, edge states, quantum anomalous Hall effect

The quantum Hall effect [1] is a transport anomaly that occurs when [2] a two-dimensional (2D) electron system has a charge gap, *i.e.* a jump in chemical potential, at a density that depends on magnetic field. It is characterized by the absence of longitudinal resistance and quantized Hall resistance. Both properties can be understood in terms of the chiral one-dimensional electron systems [3] (C1DESs) always present at quantum Hall sample edges. Although the rate at which their non-zero equilibrium currents change as chemical potential is varied is fixed by the magnetic field dependence of the gap density, other properties of C1DESs are dependent on microscopic details. In the case of GaAlAs 2D electron gas systems, for example, it has in fact been difficult to achieve a fully satisfactory understanding of chiral edge state properties because of electrostatic imperatives that force edge reconstructions [4] and cause the number of microscopic edge channels to proliferate [5]. Accurate quantization of the Hall conductance then requires [2] only that local equilibrium be established at decoupled edges of the sample.

In this Letter we address the properties of the C1DES associated with the quantum anomalous Hall effect (QAHE) [6–16] in magnetically doped topological insulator (TI) [17, 18] thin films. The appearance of a quantum Hall effect in these systems is a direct consequence of spontaneously broken time-reversal symmetry, which is also manifested by a suite of unusual magnetic [19–24], and optical [25–27] properties. We show that the C1DES associated with this quantum Hall effect is localized on the thin film sidewalls and that, in contrast to the case of GaAs quantum wells, its microscopic properties depend rather simply on film thickness, the size of the surface-state gap induced by broken time-reversal symmetry, and also on the facet dependence of surface-state Dirac velocities. Using our theory, we argue that in the absence of disorder thin films with the characteristics of samples in which the QAHE has so far been studied support a C1DES with a single chiral channel. It follows that the presence of a non-zero longitudinal resistance in most experiments [9, 24, 28–32] cannot be attributed, as is common, to the absence of local equilibrium at a multi-channel edge.

A qualitative understanding of C1DES properties can be obtained from the simplest possible 2D sidewall model. (See Refs. 33–44 for related continuum model analysis.) We assume that the sidewall has infinite extension in the $\hat{y}$ direction, thickness T in the $\hat{z}$ direction [Fig. 1(a)], and it is described by an anisotropic Dirac Hamiltonian with a mass term: $\hat{H} = i\hbar(-v_{\mathrm{D}z}\sigma_y\partial_z + v_{\mathrm{D}y}\sigma_x\partial_y) + m(z)\sigma_z$. Here $\sigma = \{\sigma_x, \sigma_y, \sigma_z\}$ is a Pauli-matrix vector that acts on spin, $m(z)$ captures the influence of exchange interactions between the top, bottom, and sidewall surface quasiparticles and the $\hat{z}$ direction of bulk magnetization, $v_{\mathrm{D}z}$ ($v_{\mathrm{D}y}$) is the vertical (horizontal) Dirac velocity. The mass is zero on the sidewall where the exchange interaction can be absorbed by a gauge change, ($m(z) = 0$ for $-T/2 < z < T/2$) and has a different sign on the top and bottom surfaces; $m(z) = m_0 > 0$ for $z > T/2$ and $m(z) = -m_0 < 0$ for $z < -T/2$, where m_0 is a constant. We find the eigenfunctions of this Hamiltonian by matching wavefunctions at the $z = \pm T/2$ boundaries [45].

The Dirac equation solutions include a set of non-chiral eigenfunctions whose role we focus on in this paper, and a chiral eigenfunction with velocity $v_{\mathrm{D}} = \sqrt{v_{\mathrm{D}z}v_{\mathrm{D}y}}$, energy $E(k) = \hbar v_{\mathrm{D}}k$, and a wavefunction that is constant inside the sidewall and decays exponentially on the top

* Now at: Nordita, KTH Royal Institute of Technology and Stockholm University, Roslagstullsbacken 23, SE-106 91 Stockholm, Sweden; anna.pertsova@su.se

and bottom surfaces [Fig. 1(d)]. The non-chiral eigenvalues are conveniently expressed in dimensionless units related to the sidewall's size-quantization energy scale: $\varepsilon = ET/\pi\hbar v_{\mathrm{D}z}$, $\mu = m_0 T/\pi\hbar v_{\mathrm{D}z}$ and $\chi = k\sqrt{v_{\mathrm{D}y}/v_{\mathrm{D}z}}T/\pi$. Because the non-chiral band energies are even functions of χ, non-chiral states always appear in equal-energy, opposite-velocity, opposite-wavevector pairs [Fig. 1(b)]. The number N_{NC} of non-chiral one-dimensional (1D) subbands that are occupied at energy ε decreases with dimensionless mass μ, as illustrated in Fig. 1(c) where the energies of non-chiral band minima, located at $\chi = 0$, are plotted as a function of μ. The wavefunctions of the non-chiral states have nodes along the $\hat{z}$ direction, with the number of nodes increasing with the energy of the state [Fig. 1(d)]. For thick films, the number of sidewall channels inside the surface-state gap is $N_{\mathrm{NC}} \sim \mu = m_0 T/\pi\hbar v_{\mathrm{D}z} \sim (m_0[\mathrm{meV}]\, T[\mathrm{nm}]/)(200\, v_{\mathrm{D}z}[10^5 \mathrm{m/s}])$. It follows that for $\mu \lesssim 1$, non-chiral states are absent across most of the surface state gap. Non-chiral channels are present across a larger fraction of the gap for thicker films, larger gaps, and smaller vertical Dirac velocities. Below we confirm these predictions of the simplified model, and obtain a numerical estimate for $v_{\mathrm{D}z}$ by performing microscopic tight-binding model calculations.

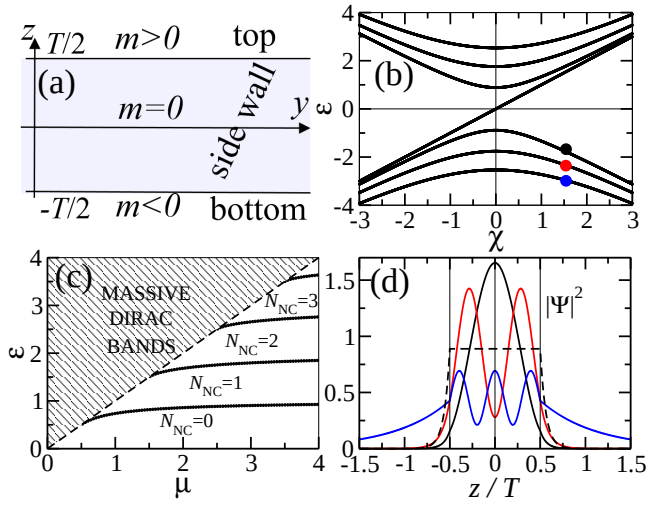

FIG. 1. (Color online) (a) A simplified model for states localized on a y-z plane sidewall. (b) Quasi 1D energy bands calculated at $\mu = 8/\pi$ with energies in $\hbar\pi v_{\mathrm{D}z}/T$ units. (c) Positive non-chiral band energies at $\chi = 0$ as a function of μ. The non-chiral bands are particle-hole symmetric. For $\epsilon > \mu$ all states extend across the top and bottom surfaces. In the limit $\mu \to \infty$ the dimensionless energies of non-chiral states approach integers. For $\epsilon < \mu$, the $\chi = 0$ band energy lines separate regions labeled by the number of non-chiral channels N_{NC} that are present. (d) Wavefunctions of the chiral state (black dashed line) and the first three negative energy non-chiral states at positive (dimensionless) momentum $\chi = 5/\pi$. The eigenvalues associated with the non-chiral wavefunctions are marked by correspondingly colored dots in (b).

In order to address transport in the QAHE regime, it is necessary to study the sidewall electronic structure microscopically [10, 34]. This will allow us: (i) to determine the velocity parameter $v_{\mathrm{D}z}$; (ii) to examine the position of the Dirac point relative to the bulk conduction and valence bands, and (iii) to shed light on relevant features that are not captured by simple continuum models, such as the hybridization between top and bottom surfaces.

We find that (i) $v_{\mathrm{D}z}$ is smaller than the top and bottom surface-state Dirac velocities, increasing the number of non-chiral sidewall channels present at a given thickness, but not drastically so in spite of the van der Waals character of the bonding between quintile layers (QLs), (ii) exchange coupling on its own does not shift the position of the Dirac point within the surface-state gap and (iii) hybridization between top and bottom surfaces sets the minimum exchange interaction strength required for a QAHE at 90 meV for 3QL and at 0.01 meV for 5QL films. The surprisingly large value of $v_{\mathrm{D}z}$ simplifies the QAHE in TI thin films and improves prospects for accurate quantum Hall effects and for future experimental studies of sidewall state properties.

We focus on Bi_2Se_3 TI [46] whose electronic structure can be described by a sp^3 tight-binding model with parameters obtained by fitting to *ab initio* calculations [47, 48]. We assume that a ferromagnetic state is achieved by magnetic doping. The systems that we have in mind are Cr or Fe-doped Bi_2Se_3 or $(Bi,Sb)_2Te_3$. Here substitutional dopants only establish a ferromagnetic insulating state, with minor modifications of the host electronic structure, without introducing free carriers [8]. We model a homogeneous perpendicular magnetization by an exchange field B_{ex} expressed in energy units and oriented perpendicular to the (111) surface. In real samples the effective exchange field is certainly more complicated than the homogeneous field used in our model. However, short-range exchange fluctuations are less important for generating a surface-state gap than the long-range properties of the magnetization, which are adequately captured by a homogeneous field. To test this hypothesis, we considered an inhomogeneous exchange field which is distributed predominantly on Bi atoms but its value is adjusted to produce the same surface-state gap. We find that the electronic structure of the sidewall states is mostly unchanged [45].

To extract the facet-dependent Dirac velocities we first consider the thin-film geometry. For the Se (111) surface-layer facet [Fig. 2(c)], we find that the Dirac cone is isotropic with velocity $v_{\mathrm{D}}^0 \approx 5.0 \times 10^5$ m/s. For the mixed Bi/Se $(\bar{1}10)$ sidewall facet [Fig. 2(b)] [49], the Dirac cone is strongly anisotropic with $v_{\mathrm{D}y} \approx 4.7 \times 10^5$ m/s and $v_{\mathrm{D}z} \approx 2.3 \times 10^5$ m/s. (The values are accurate within the quoted digits [45]). We then turn to the ribbon geometry [Fig. 2(a)] in order to identify the sidewall states active in QAHE transport experiments. The ribbon is infinite in the $\hat{y}$ direction, the direction of longitudinal transport, has a thickness T in the $\hat{z}$ direction approxi-

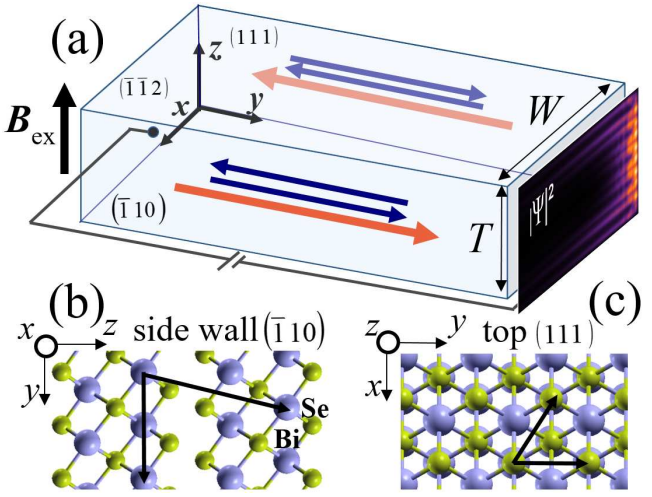

FIG. 2. (Color online) (a) Bi_2Se_3 nanoribbon with thickness T and width W. The thick red arrows represent currents carried by ballistic chiral edge states, while the thin blue arrows represent currents carried by ballistic non-chiral edge states. The sidewall localization property of chiral states is reflected by the illustrated $|\Psi|^2$ probability density distribution across the ribbon cross section. Top views of the $(\bar{1}10)$ sidewall (b) and the (111) top and bottom surface layers (c), with black arrows for 2D crystal unit vectors.

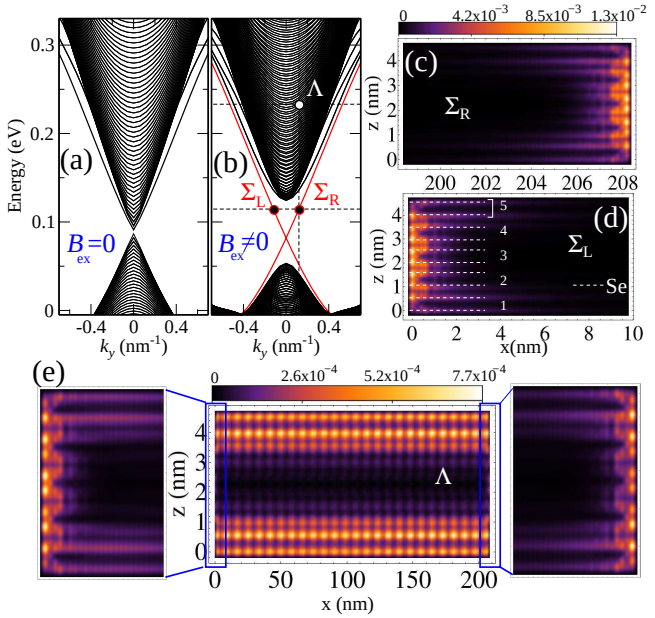

FIG. 3. (Color online) Bandstructure of a Bi_2Se_3 nanoribbon with $T = 5$QL and $W = 208$ nm for $B_{ex} = 0$ (a) and $B_{ex} = 0.16$ eV (b). Chiral edge states are shown in red in panel (b). Spatial distribution of the wavefunction across the ribbon cross-section for a right-goer state Σ_R (c) and a left-goer state Σ_L (d) with energy ≈ 0.11 eV [dashed line in (b)], and a non-chiral state Λ (e) with energy ≈ 0.23 eV [white circle in (b)]. The dashed lines in (d) mark the positions of the outermost Se layers in each QL. In (c) and (d) only the ribbon edges are shown.

mately equal to 1 nm per QL, and a finite width W in the $\hat{x}$ direction. Results for ribbons with $T = 5$QL and $W = 208$ nm are presented in Fig. 3.

At $B_{ex} = 0$ the low-energy states consist of discrete quasi 1D channels separated in energy by $\sim \hbar\pi v_D/(T + W)$ [37] as illustrated in Fig. 3(a). Wavefunctions at energies within the bulk gap (between 0 and 0.4 eV for a 5QL film), are distributed over all four facets of the ribbon at $k = 0$, but because of the Dirac velocity mismatch tend to localize either on sidewall or on surface facets at $k \neq 0$. At $B_{ex} = 0.16$eV a gap opens and is bridged by a pair of chiral edge states [Fig. 3(b)]. The size of the gap is smaller than the exchange coupling energy because, in contrast to the toy model, the quasiparticles have mixed spin character even at $k = 0$ and g-factors that are smaller than 2. The gap is 70 meV and can be identified with the gap $2m_0$ in the toy model. It follows that $B_{ex} = 0.16$eV corresponds to $m_0 = 35$ meV, in agreement with typical experimental estimates. At a given energy, the negative-velocity (Σ_L) and positive-velocity (Σ_R) chiral states are localized on the opposite sidewalls [see Fig. 3(c) and (d)]. The value of the chiral-state velocity is $\approx 4.2 \times 10^5$ m/s [45], which is consistent with the estimate provided by the toy-model expression $v_D = \sqrt{v_{Dz} v_{Dy}} \approx 3.3 \times 10^5$ m/s (evaluated for v_{Dz} and v_{Dy} quoted above). Both states are spin-polarized in the direction of the exchange field.

Non-chiral channels appear only at energies outside of the surface-state gap. A typical non-chiral state, illustrated in Fig. 3(e) (Λ), has weight on both sidewalls and on the top and bottom surfaces. The absence of sidewall-localized non-chiral channels in these calculations can be understood by comparing with the toy model and using the microscopically calculated value for v_{Dz} to evaluate the dimensionless gap parameter. We find that for the thickness and exchange interaction strength of this representative microscopic calculation $\mu \sim 0.3$ [45], consistent with the $N_{NC} = 0$ electronic structure of Fig. 3(b). Non-chiral channels appear at energies inside the surface-state gap only for thicker films or stronger exchange splitting. Our sidewall toy model does not account for the hybridization between top and bottom surfaces which, in very thin films, controls a transition between quantum Hall and topologically trivial states [8]. The hybridization scale is negligible compared to typical exchange energy scales in 5QL films, but not in 3QL films whose properties are summarized in Fig. 4. Hybridization opens a sizable surface-state gap in 3QL films at $B_{ex} = 0$. This time-reversed ground state is a 2D TI and supports helical edge states. The gap decreases in size with increasing B_{ex} and vanishes at $B_{ex} = B_{ex}^{cr}$. For $B_{ex} > B_{ex}^{cr}$ the order of the lowest 2D subbands is reversed, causing a transition to the QAHE phase [45], and the gap size then increases with B_{ex}. We find that $B_{ex}^{cr} \approx 90$ meV for 3QL and that $B_{ex}^{cr} \approx 0.01$ meV for 5QL. Although remnants

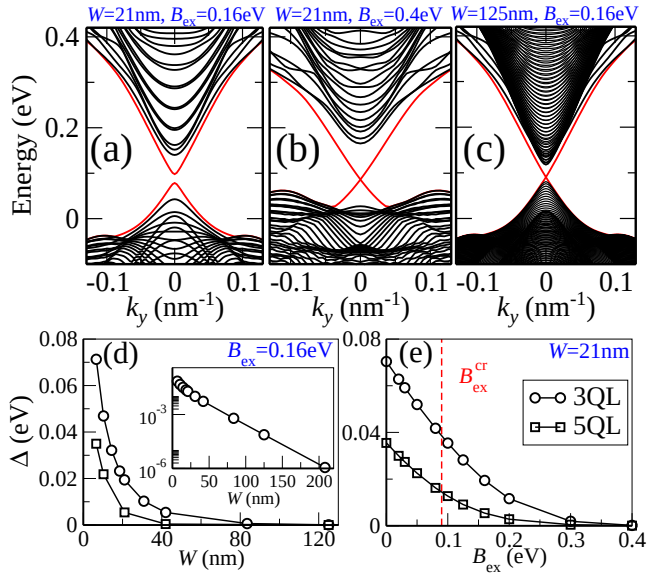

FIG. 4. (Color online) Bandstructure of a Bi_2Se_3 nanoribbon with $T = 3$QL for $W = 21$ nm and $B_{ex} = 0.16$ eV (a), $W = 21$ nm and $B_{ex} = 0.4$ eV (b), and $W = 125$ nm and $B_{ex} = 0.16$ eV (c). Chiral edge states are shown in red. (d) Chiral state avoided crossing gap for $T = 3$QL (circles) and $T = 5$QL (squares) as a function of W for B_{ex}=0.16 eV. The inset shows the logarithm of the gap for 3QL films over a larger range of W's. (e) Gap as a function of B_{ex} for a fixed $W = 21$ nm in the same two cases. The vertical dashed line marks the critical exchange field ($B_{ex}^{cr} \approx 0.09$ eV) for 3QL.

of the $B_{ex} = 0$ helical edge states can complicate the edge electronic structure when $B_{ex} \lesssim B_{ex}^{cr}$, our microscopic calculations demonstrate that no trace is present for $B_{ex} \gg B_{ex}^{cr}$ where only the chiral edge modes survive.

For finite-width ribbons there is a gap in the spectrum for $B_{ex} > B_{ex}^{cr}$ because of the avoided crossing between edge states localized on opposite sidewalls. This gap decreases in size both with increasing B_{ex} [Fig. 4(b)] or W [Fig. 4(c)]. For a fixed exchange field $B_{ex} > B_{ex}^{cr}$ the gap decreases exponentially with W [Fig. 4(d)], whereas for $B_{ex} < B_{ex}^{cr}$, the gap approaches a finite value as $W \to \infty$. By fitting the W dependence of the gap to an exponential-decay law we estimate that the localization length of the chiral edge state at $B_{ex} = 0.16$ eV is ≈ 18.6 nm for 3QL and ≈ 8.2 nm for 5QL. Since typical experimental samples used in QAHE studies have widths of hundreds of μm, direct coupling between opposite edges is negligible in the absence of disorder.

Experimental QAHE measurements have so far been performed mainly on films with thicknesses in the range between 5 and 10QL. Because the vertical sidewall Dirac velocity, which characterizes a direction in which electrons hop between Bi and chalcogen layers, is only a few times smaller than in-plane Dirac velocities, the 10QL maximum thickness is not sufficient to support non-chiral edge modes. At the same time, hybridization between top and bottom surfaces at the minimum 5QL thickness is very much weaker than typical exchange fields. For this reason, we conclude that the sidewalls of the typical samples do not support either helical edge states that are a remnant of $B_{ex} = 0$ 2D TI states, or the non-chiral sidewall states [10] expected in thicker films. This is one of the central results of our study, which accounts for the nearly perfectly quantized anomalous Hall conductance found in experiment.

Because the sidewall spectrum consists of a single chiral channel, it is not possible to explain the commonly observed finite longitudinal resistances by assuming a failure to establish local equilibrium on a multi-channel edge. A more likely explanation, in our view, is that potential disorder causes the local Fermi level to sweep across the surface-state gap. The relatively high-velocity 1D chiral sidewall states have negligible density of states. They therefore can do little on their own to screen inevitable spatial variations in external electric fields that induce relative shifts in the Dirac cones of top and bottom surfaces, or external potentials that induce common shifts in the Dirac cones of the two surfaces.

Fluctuations that bring the surface states of large-area top or bottom facets to the Fermi level, provide a mechanism for 2D dissipative transport in some parts of the system. The consequences for transport are similar to those of non-chiral edge states. In this case however, the dissipation is not an intrinsic property of the sidewall states, and should be weakened when potential fluctuations are reduced. This suggests that smaller longitudinal resistances and more accurate quantization can be achieved in higher quality samples with less uncontrolled and uncharacterized disorder.

According to our theory, thicker samples will eventually support non-chiral edge modes, which can lead to an increased longitudinal dissipation. However, disorder in this case can also support dissipationless transport by localizing non-chiral channels and establishing local equilibrium on spatially separated sidewall segments. Hence a larger number of channels on the sidewalls can increase the degree to which disorder is screened and help broaden the gate voltage range over which nearly pure sidewall transport can be established.

This work was supported by the Faculty of Technology at Linnaeus University and by the Swedish Research Council under Grant Number: 621-2014-4785. AHM was supported by the Welch Foundation under grant F-1473 and by SHINES, an Energy Frontier Research Center funded by the U.S. Department of Energy (DoE), Office of Science, Basic Energy Science (BES) under award DE-SC0012670. AHM acknowledges valuable interactions with Yabin Fan, Massoud Masir, Pramay Upadhyaya, Kang Wang, Fengcheng Wu and Fei Xue. Computational resources have been provided by the Lunarc center for scientific and technical computing at Lund University.

[1] K. v. Klitzing, G. Dorda, and M. Pepper, Phys. Rev. Lett. **45**, 494 (1980).
[2] A. H. MacDonald, Mesoscopic Quantum Physics **61**, 659 (1995).
[3] X. Wen, Phys. Rev. B **43**, 11025 (1991).
[4] C. d. C. Chamon and X. G. Wen, Phys. Rev. B **49**, 8227 (1994).
[5] D. B. Chklovskii, B. I. Shklovskii, and L. I. Glazman, Phys. Rev. B **46**, 4026 (1992).
[6] F. D. M. Haldane, Phys. Rev. Lett. **61**, 2015 (1988).
[7] C.-X. Liu, X.-L. Qi, X. Dai, Z. Fang, and S.-C. Zhang, Phys. Rev. Lett. **101**, 146802 (2008).
[8] R. Yu, W. Zhang, H.-J. Zhang, S.-C. Zhang, X. Dai, and Z. Fang, Science **329**, 61 (2010).
[9] C.-Z. Chang, J. Zhang, X. Feng, J. Shen, Z. Zhang, M. Guo, K. Li, Y. Ou, P. Wei, L.-L. Wang, Z.-Q. Ji, Y. Feng, S. Ji, X. Chen, J. Jia, X. Dai, Z. Fang, S.-C. Zhang, K. He, Y. Wang, L. Lu, X.-C. Ma, and Q.-K. Xue, Science **340**, 167 (2013).
[10] J. Wang, B. Lian, H. Zhang, and S.-C. Zhang, Phys. Rev. Lett. **111**, 086803 (2013).
[11] X.-L. Qi, Y.-S. Wu, and S.-C. Zhang, Phys. Rev. B **74**, 085308 (2006).
[12] X.-L. Qi, T. L. Hughes, and S.-C. Zhang, Phys. Rev. B **78**, 195424 (2008).
[13] K. Nomura and N. Nagaosa, Phys. Rev. Lett. **106**, 166802 (2011).
[14] K. He, Y. Wang, and Q.-K. Xue, National Science Review (2013), 10.1093/nsr/nwt029.
[15] X. Kou, Y. Fan, M. Lang, P. Upadhyaya, and K. L. Wang, Solid State Communications **215216**, 34 (2015).
[16] H. Weng, R. Yu, X. Hu, X. Dai, and Z. Fang, Advances in Physics **64**, 227 (2015).
[17] M. Z. Hasan and C. L. Kane, Rev. Mod. Phys. **82**, 3045 (2010).
[18] X.-L. Qi and S.-C. Zhang, Rev. Mod. Phys. **83**, 1057 (2011).
[19] Y. Tserkovnyak and D. Loss, Phys. Rev. Lett. **108**, 187201 (2012).
[20] J.-J. Zhu, D.-X. Yao, S.-C. Zhang, and K. Chang, Phys. Rev. Lett. **106**, 097201 (2011).
[21] Y. L. Chen, J.-H. Chu, J. G. Analytis, Z. K. Liu, K. Igarashi, H.-H. Kuo, X. L. Qi, S. K. Mo, R. G. Moore, D. H. Lu, M. Hashimoto, T. Sasagawa, S. C. Zhang, I. R. Fisher, Z. Hussain, and Z. X. Shen, Science **329**, 659 (2010).
[22] J. G. Checkelsky, J. Ye, Y. Onose, and Y. Tokura, Nature Physics **8**, 729 (2012).
[23] S.-Y. Xu, M. Neupane, C. Liu, D. Zhang, A. Richardella, L. A. Wray, N. Alidoust, M. Leandersson, T. Balasubramanian, J. Sánchez-Barriga, O. Rader, G. Landolt, B. Slomski, J. H. Dil, J. Osterwalder, T.-R. Chang, H.-T. Jeng, H. Lin, A. Bansil, N. Samarth, and M. Z. Hasan, Nature Physics **8**, 616 (2012).
[24] S. Grauer, S. Schreyeck, M. Winnerlein, K. Brunner, C. Gould, and L. W. Molenkamp, Phys. Rev. B **92**, 201304 (2015).
[25] W.-K. Tse and A. H. MacDonald, Phys. Rev. Lett. **105**, 057401 (2010).
[26] A. G. Mal'shukov, H. Skarsvåg, and A. Brataas, Phys. Rev. B **88**, 245122 (2013).
[27] M. Lasia and L. Brey, Phys. Rev. B **90**, 075417 (2014).
[28] J. Checkelsky, R. Yoshimi, A. Tsukazaki, K. S. Takahashi, Y. Kozuka, J. Falson, M. Kawasaki, and Y. Tokura, Nature Physics **10**, 731 (2014).
[29] X. Kou, S.-T. Guo, Y. Fan, L. Pan, M. Lang, Y. Jiang, Q. Shao, T. Nie, K. Murata, J. Tang, Y. Wang, L. He, T.-K. Lee, W.-L. Lee, and K. L. Wang, Phys. Rev. Lett. **113**, 137201 (2014).
[30] A. J. Bestwick, E. J. Fox, X. Kou, L. Pan, K. L. Wang, and D. Goldhaber-Gordon, Phys. Rev. Lett. **114**, 187201 (2015).
[31] C.-Z. Chang, W. Zhao, D. Y. Kim, H. Zhang, B. A. Assaf, D. Heiman, S.-C. Zhang, C. Liu, M. H. W. Chan, and J. S. Moodera, Nature Physics **14**, 473 (2015).
[32] C.-Z. Chang, W. Zhao, D. Y. Kim, P. Wei, J. K. Jain, C. Liu, M. H. W. Chan, and J. S. Moodera, Phys. Rev. Lett. **115**, 057206 (2015).
[33] W.-K. Lou, F. Cheng, and J. Li, Journal of Applied Physics **110**, 093714 (2011).
[34] F. W. Chen, L. A. Jauregui, Y. Tan, M. Manfra, G. Klimeck, Y. P. Chen, and T. Kubis, Applied Physics Letters **107**, 121605 (2015).
[35] O. Deb, A. Soori, and D. Sen, Journal of Physics: Condensed Matter **26**, 315009 (2014).
[36] Y.-Y. Zhang, X.-R. Wang, and X. C. Xie, Journal of Physics: Condensed Matter **24**, 015004 (2012).
[37] J. H. Bardarson, P. W. Brouwer, and J. E. Moore, Phys. Rev. Lett. **105**, 156803 (2010).
[38] G. Rosenberg, H.-M. Guo, and M. Franz, Phys. Rev. B **82**, 041104 (2010).
[39] Y. Zhang and A. Vishwanath, Phys. Rev. Lett. **105**, 206601 (2010).
[40] K. Chang and W.-K. Lou, Phys. Rev. Lett. **106**, 206802 (2011).
[41] L. Brey and H. A. Fertig, Phys. Rev. B **89**, 085305 (2014).
[42] S. Acero, L. Brey, W. J. Herrera, and A. L. Yeyati, Phys. Rev. B **92**, 235445 (2015).
[43] F. Zhang, C. L. Kane, and E. J. Mele, Phys. Rev. Lett. **110**, 046404 (2013).
[44] F. Zhang, C. L. Kane, and E. J. Mele, Phys. Rev. B **86**, 081303 (2012).
[45] See Supplemental Material for (i) a detailed description of the sidewall toy model and its parameters, (ii) a discussion of the exchange-field driven topological phase transition in ultrathin TI thin films, and (iii) a discussion of the effects of a non-uniform exchange field on the edge spectrum.
[46] D. Hsieh, Y. Xia, D. Qian, L. Wray, J. H. Dil, F. Meier, J. Osterwalder, L. Patthey, J. G. Checkelsky, N. P. Ong, A. V. Fedorov, H. Lin, A. Bansil, D. Grauer, Y. S. Hor, R. J. Cava, and M. Z. Hasan, Nature **460**, 1101 (2009).
[47] K. Kobayashi, Phys. Rev. B **84**, 205424 (2011).
[48] A. Pertsova and C. M. Canali, New Journal of Physics **16**, 063022 (2014).
[49] Y.-L. Lee, H. C. Park, J. Ihm, and Y.-W. Son, Proceedings of the National Academy of Sciences **112**, 11514 (2015).